Hybrid Piezoresistive 2D MoS2/PEGDA/PANI Covalent Hydrogels for the Sensing of LowtoMedium Pressure

small structures
www.small-structures.com

Hybrid Piezoresistive 2D MoS_2/PEGDA/PANI Covalent Hydrogels for the Sensing of Low-to-Medium Pressure

*Sara Domenici, Sara Micheli, Matteo Crisci, Marcus Rohnke, Hannes Hergert, Marco Allione, Mengjiao Wang, Bernd Smarlsy, Peter J. Klar, Francesco Lamberti, Elisa Cimetta, Luca Ceseracciu, and Teresa Gatti**

Wearable technologies are attracting increasing attention in the materials science field, prompting a quest for active components with beneficial functional attributes whilst ensuring human and environmental safety. Hydrogels are highly biocompatible platforms with interesting mechanical properties, which can be exploited for the construction of strain sensors. In order to improve the directionality of their strain response and combine it with electrical properties to fabricate piezoresistive devices, it is possible to incorporate various types of nanofillers within the polymeric network of the hydrogels. 2D materials are ideal nanofillers thanks to their intrinsic two-dimensional anisotropy and unique electronic properties. Herein, the covalent functionalization of 2D 1T-MoS_2 is exploited to build robust hybrid cross-linked networks with a polyethylene glycol diacrylate gel (PEGDA). The conductivity of this nanocomposite is also further improved by inducing the interfacial polymerization of aniline. The resulting free-standing samples demonstrate a linear and highly reversible piezoresistive response in a pressure range compatible with that of peripheral blood, while also featuring good compatibility with human skin cells, thereby making them interesting options for incorporation into wearable strain sensors.

1. Introduction

Wearable devices are a class of electronic systems designed to be worn on the user's body and are commonly found in the form of accessories, such as smart watches, glasses and headsets, or incorporated into clothing.[1–4] The continuous research on electronics, biocompatible materials and nanomaterials has led to the design of new generations of wearables that can be employed in direct physical contact with the body of the user as attachable, or even implantable devices.[5] These devices hold promise for clinical uses, as their primary benefit lies in offering real-time, non-invasive health monitoring and precise sensing of physiological functions.[6] Currently, the major challenge for this new technology is the identification of stretchable and skin-adhesive materials to assemble devices that can continuously and comfortably monitor human vital signs and activity without being disrupted by the movement of the user,[5] whilst also ensuring biological compatibility.[7] Benefiting from the compatibility with

S. Domenici, M. Allione, M. Wang, T. Gatti
Department of Applied Science and Technology
Politecnico di Torino
C.so Duca degli Abruzzi 24, 10129 Torino, Italy
E-mail: teresa.gatti@polito.it

S. Domenici, M. Crisci, M. Rohnke, H. Hergert, B. Smarlsy, P. J. Klar, T. Gatti
Center for Materials Research
Justus-Liebig University
Heinrich-Buff-Ring 16-17, 35392 Giessen, Germany

S. Micheli, E. Cimetta
Department of Industrial Engineering
University of Padova
Via Marzolo 9, 35131 Padova, Italy

The ORCID identification number(s) for the author(s) of this article can be found under https://doi.org/10.1002/sstr.202400131.

DOI: 10.1002/sstr.202400131

M. Crisci, M. Rohnke, B. Smarlsy
Institute of Physical Chemistry
Justus Liebig University
Heinrich-Buff-Ring 17, 35392 Giessen, Germany

H. Hergert, P. J. Klar
Institute of Experimental Physics I
Justus Liebig University
Heinrich-Buff-Ring 16, 35392 Giessen, Germany

F. Lamberti
Department of Chemical Sciences
University of Padova
Via Marzolo 1, 35131 Padova, Italy

L. Ceseracciu
Materials Characterization Facility
Istituto Italiano di Tecnologia
Via Morego 30, 16163 Genova, Italy

wet environments, and comfort deriving from their intrinsic softness, hydrogels are widely employed in the field of bioelectronics such as wearable devices,[8] electronic skins,[9] health monitoring[10,11] and motion detection.[12] However, pure hydrogels are typically isotropic materials, and the trigger of a response to strain stimuli is unlikely. Hydrogels are thus usually used as water-insoluble tridimensional networks of polymeric chains to contain and support an anisotropic micro/nanostructure, which will generate mismatch stress for a strain sensing under specific stimuli.[13] However, the appropriate integration of sensing materials into hydrogels is often a challenge due to the incompatibility between materials, structures, and gelation methods.[13,14]

Two-dimensional (2D) materials, having intrinsically anisotropic structures[15] are the most promising and have been widely researched.[16] In the context of strain sensors, the incorporation of 2D nanofillers in hydrogel matrices has already been explored. In many interesting works, highly conductive MXene[17–20] and graphene oxide (GO) nanoflakes[21] were embedded in polymeric matrixes to yield conductive hydrogel-based sensors with excellent mechanical properties and high-pressure sensitivity. Amongst 2D materials, molybdenum disulfide (MoS_2), a transition metal dichalcogenide (TMD), has attracted interest for fundamental studies and applications in biomedicine[22] due to its low cytotoxicity and its biocompatibility.[23,24] This 2D-TMD is usually produced with different methodologies, with liquid phase exfoliation (LPE) being particularly appealing due to its facile scalability and low environmental impact,[25,26] thus leading to large quantities of the desired nanomaterial in the form of stable colloidal ink. 2D MoS_2 nanoflakes produced via LPE can be then integrated into hydrogels, leading to hybrid materials with improved structural characteristics, while also adding distinct properties to the final hybrid material, such as electrical properties, and still maintaining their softness, their flexibility[27] and biocompatibility.[28] Nevertheless, it is not always clear how the 2D nanomaterial usually interacts with the other components of a similar hybrid system: adsorption and weak interaction are often not enough to ensure good performance and stability to phase-separation in such composites. For this issue, pre-functionalization of the 2D material can be a possible solution to fine-tune and orient the type of interactions between nanofillers and polymeric gel matrices. This challenge has already been tackled in other works. For example, Pan et al.[29] covalently grafted olefin molecules on chemically exfoliated MoS_2 (ce-MoS_2) and the modified nanofiller was used both as a catalyst for acrylamide polymerization and as a cross-linker. Another innovative approach was applied by Xu et al.[27] In their work, the sulfur defects of ce-MoS_2 were exploited to conjugate a 4-arm poly(ethylene glycol) thiol molecule, which then reacted with gelatin methacrylate in a thiol-ene click reaction to yield a hydrogel network.

The integration of different polymers can improve the toughness and stability of these composites, while also contributing to other functional properties. As an example, the integration of conductive polymers in gel matrices is a promising method to modulate their electrical response.[30] This integration should occur in situ after the primary matrix is obtained since the presence of the conducting polymer particles in the primary mixture can limit the degree of crosslinking of the matrix. Moreover, in light-triggered polymerizations, the conductive polymer can also make the mixture opaque to UV light.[31] One interesting example of this strategy in the context of strain sensors was carried out by He et al.[32] In their work, a conductive hydrogel network composed of poly(acrylamide-co-acrylic acid) and phosphorylated cellulose nanofibrils was achieved with the in-situ formation of polypyrrole (PPy) chains induced by Fe^{3+} ions. The combination of Fe^{3+} ions and PPy chains enabled to construct a stable conductive network.

In this work, we exploit LPE and covalent grafting to incorporate functionalized 1T-MoS_2 few-layers nanoflakes[33] into a polyethylene glycol diacrylate (PEGDA) hydrogel network. We further tune the resistivity of the soft hybrid material by in-situ triggering the interfacial polymerization of the conductive polymer, polyaniline (PANI),[34] both for its electronic properties and biocompatibility.[35] Through this approach we fabricate self-standing thick hybrid hydrogel samples, demonstrating a linear and reversible piezoresistive response up to 50% strain in the 0–9.5 kPa pressure range, excellently matching peripheral blood pressure values. Our novel hybrid material holds great promise as a platform for building strain sensor devices for wearable technologies.

2. Results and Discussion

The first step to synthesize a covalently cross-linked hybrid hydrogel was the preparation of 2D 1T-MoS_2 functionalized with organic moieties. The 1T-phase of MoS_2 was chosen over the 2H phase for its easier functionalization toward electrophilic reaction,[33,36] and better conductive properties. The overall process of fabricating functionalized 1T-MoS_2 is depicted in **Figure 1**a. Bulk MoS_2 was chemically exfoliated *via* lithium-ions intercalation, followed by a tip sonication in water to perform LPE.[37] The functionalization reaction was then carried out in N-methyl-2-pyrrolidone (NMP) through an in-situ Tour-type arylation protocol.[38,39] This process yielded few-layers 1T-MoS_2 bearing pendant p-methoxyphenyl substituents, *f*-MoS_2(–OCH_3). Detailed procedures for the preparation of inks of chemically exfoliated MoS_2 are described in the Experimental Section. Briefly, the result of the intercalation of Li^+ ions and LPE through tip sonication was a black aqueous suspension of 1T-MoS_2 (Figure S1, Supporting Information) containing nanosheets up to 500 nm in lateral size and a few layers thick, as shown by the transmission electron microscopy (TEM) of a representative sample in Figure S2, Supporting Information. High resolution (HR-TEM) images highlight the presence of the typical octahedral structure of the 1T phase, as well as 2H-MoS_2 in other areas on a single flake with its characteristic hexagonal structure (inset magnifications in Figure 1b). In addition, the measured zeta potential of the obtained aqueous suspension is of −40 mV, indicating high stability with numerous negative charges on the surface of the nanoflakes.

After LPE, the covalent functionalization of the nanosheets was carried out using a *para*-substituted aniline, p-anisidine, exploiting the in-situ formation of its aryl diazonium salt through a reaction with isoamyl nitrite and the grafting on the electron-rich substrate via the Tour reaction.[40] Products from the two steps, Li-mediated LPE and functionalization, were characterized using different analytical techniques and then compared. The

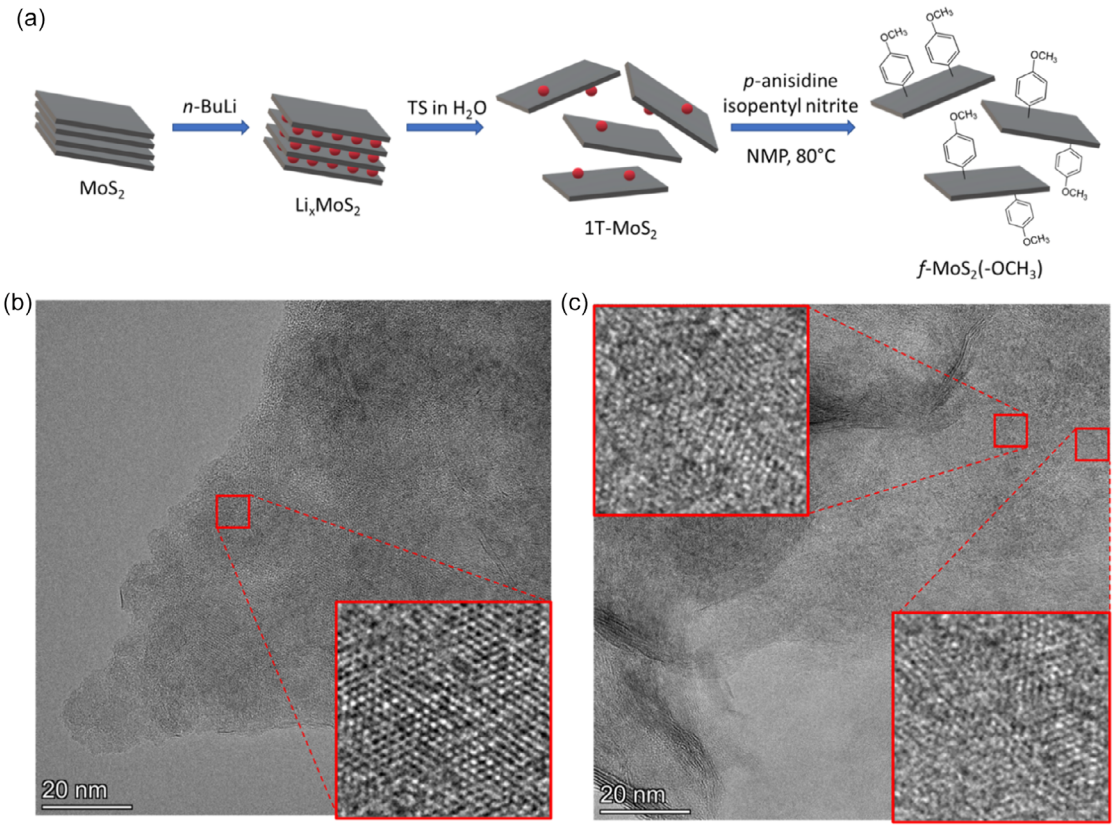

Figure 1. a) Sketch of the Li-intercalation-LPE-covalent functionalization process used to produce *f*-MoS_2(–OCH_3) nanoflakes suitable for covalent cross-linking with a hydrogel network. HR-TEM images of b) LPE 1T-MoS_2 and c) *f*-MoS_2(–OCH_3). Inset magnifications show the distorted octahedral structure of 1T-MoS_2, as well as hexagonal domains of 2H-MoS_2.

Raman spectrum of the 1T-MoS_2 shows the typical J_1, J_2 and J_3 bands at ≈157, 225 and 330 cm^{-1},[41,42] characteristic of this phase of the TMD (Figure S3, Supporting Information). UV-Vis spectra were also compared with an aqueous suspension of exfoliated 2H-MoS_2 prepared following the procedure reported in a previous work *via* surfactant-assisted LPE in water.[43] The absorption spectrum of the exfoliated 2H-phase shows two peaks from direct excitonic transitions at 608 and 667 nm, and two related to the optical transitions from the deep valence band to the conduction band around 395 and 446 nm.[44] On the other hand, the spectrum of the 1T-phase in water has no significant absorption bands, but instead, a monotonic change showing its metallic character[45] (Figure S4, Supporting Information). The product of the functionalization, *f*-MoS_2(–OCH_3), has a spectrum similar to that of the 1T-phase suspension, but with the characteristic excitonic peaks relative to the semiconducting phase of MoS_2. This may be attributed to the grafting of molecules on the S plane, promoting a structural rearrangement and thus partially restoring the semiconducting phase.[46]

The covalent functionalization of the TMD nanoflakes was further studied to identify their main components by analyzing XPS spectra through deconvolution (**Figure 2**c–f). Specifically, the Mo 3*d* spectra showed a significant increase in the peak at around 229.3 and 232.3 eV after functionalization, which was attributed to the 2H-phase. At the same time, the peaks at 228.2 and 231.3 eV decreased, corresponding to the 1T-phase,[47,48] supporting the hypothesis of a partial transition of the material back to the thermodynamically stable 2H semiconducting phase. The presence of oxide (mostly MoO_3) was also detected, likely generated after air exposure during the different steps of the processes. XPS spectra also enabled to calculate the relative amount of the two phases (**Table 1**). These data further confirmed that the chemical exfoliation process did not reach a 100% yield in 1T-phase and that after functionalization there is a partial reconversion from the 1T component back to the thermodynamically stable 2H one.

HR-TEM analysis offers a closer examination at the atomic scale in the MoS_2 lattice, revealing that both phases are present in the functionalized material without significant structural alterations. The inset in Figure 1c is a representative HR-TEM image of *f*-MoS_2(–OCH_3), in which the distorted octahedral coordinated structure of 1T-MoS_2 is still visible within the flake together with the 2H-phase, confirming the fabrication of a mixed-phase nanomaterial. Thermogravimetric analysis (TGA) was employed to estimate the degree of functionalization in *f*-MoS_2(–OCH_3). TGA revealed a ≈5% mass reduction between 200 and 400 °C (Figure 2a), typical of organic matter loss. Using the molar masses of anisole and MoS_2, and assuming that the weight loss stems solely from the organic moieties, we estimated a degree of functionalization per S atom of ≈4%,[36] in agreement with

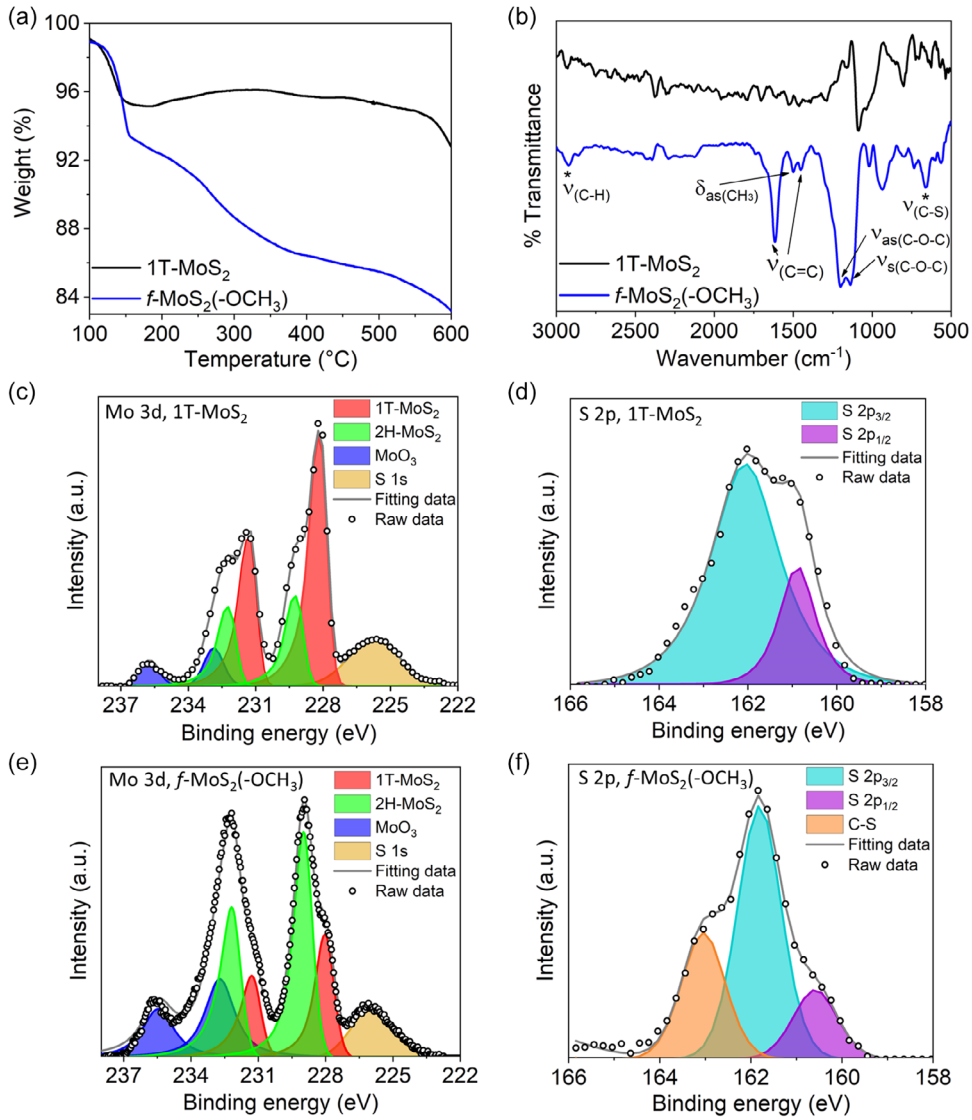

Figure 2. Physico-chemical characterization of LPE 1T-MoS_2 and of *f*-MoS_2(–OCH_3). a) Thermogravimetric weight loss comparison between *f*-MoS_2(–OCH_3) and 1T-MoS_2. b) FTIR spectra of *f*-MoS_2(–OCH_3) and 1T-MoS_2. XPS spectra of c,d) 1T-MoS_2 and of e,f) *f*-MoS_2(–OCH_3) with high resolution scans of Mo 3*d* and S 2*p*.

Table 1. Peak positions and calculated percentages of the different contributions in the XPS spectra (high resolution scan of Mo 3*d*) for the two species.

Sample name	Component	Fitted peak position [eV]		Calculated percentage [%]
		$3d_{3/2}$	$3d_{5/2}$	
1T-MoS_2	1T-MoS_2	231.3	228.2	63.4%
	2H-MoS_2	232.3	229.3	26.8%
	MoO_3	235.7	232.8	9.8%
f-MoS_2(–OCH_3)	1T-MoS_2	231.3	228.0	23.3%
	2H-MoS_2	232.2	229.0	42.9%
	MoO_3	235.5	232.7	33.8%

findings in literature.[33,36] XPS was employed to further confirm the covalent functionalization, revealing a peak at 163.2 eV in the S 2*p* spectra of *f*-MoS_2(–OCH_3) attributed to the C—S bond.[49,50] Such contribution was absent in the pristine 1T-MoS_2 sample, where only the peaks related to metal-sulfur bonds (≈162 eV) and to sulfate moieties (≈169–170 eV) were detected from deconvolution.

Finally, we also investigated the presence of the C—S bond through Fourier Transformed Infrared (FTIR) spectroscopy. Unlike the pristine TMD, *f*-MoS_2(–OCH_3) spectra exhibited a vibration at ≈670 cm^{-1}, attributed to the stretching of the S—C bond, thus confirming the covalent grafting of the p-anisidine moieties on to the S atoms of the flakes[33] (Figure 2b). Additionally, the stretching vibrations of the aromatic

C═C and C─H bonds were detected from the peaks at ≈1610 and 2930 cm^{-1}, respectively. Similarly, we identified the characteristic peaks of the functional methoxy group: the asymmetric bending of $–CH_3$ at 1440 cm^{-1} and the symmetric and asymmetric stretching vibrations of the C─O─C bond at 1140 and 1200 cm^{-1}, respectively. Moreover, broad signals between 1100 and 1700 cm^{-1} were observed through Raman spectroscopy and could be assigned to C═C stretching of the aromatic organic moieties[51] (Figure S5, Supporting Information).

As detailed in the Experimental Section, we tailored the synthesis of the soft hydrogels to optimize their flexibility, mechanical and chemical stability, and swelling capacity, using UV light-triggered polymerization. Given the presence of organic moieties on the surface of the flakes, the gels were expected to form as chemically cross-linked hybrid materials, exploiting the formation of covalent bonds between the organic and the inorganic components. In this scenario, during the synthesis of the hydrogels in the presence of the inorganic TMD nanofillers, polymer radicals could graft onto the surface of the flakes by covalently attaching in *ortho*-position to the p-anisidine pendant moieties,[52,53] as depicted **Figure 3**a. With covalent functionalization, the 2D nanomaterial is effectively embedded in the matrix

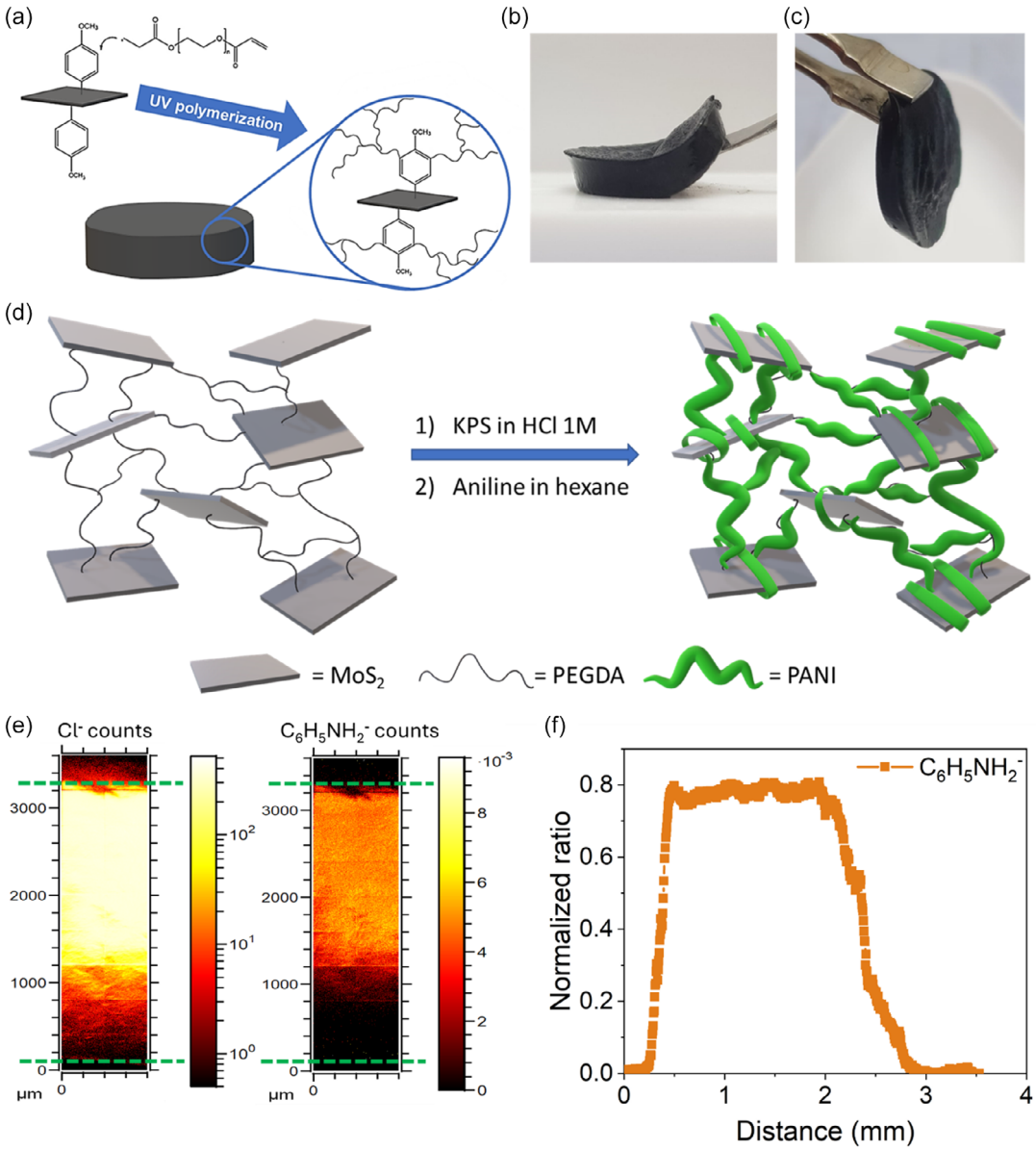

Figure 3. Preparation of the ternary *f*-MoS_2(–OCH_3)/PEGDA/PANI covalent hydrogels. a) Sketch illustrating the covalent grafting of PEGDA chains to *f*-MoS_2(–OCH_3) and of the UV-polymerization/cross-linking process to produce the hydrogels. b) Images of the self-standing binary and c) ternary gel samples (approximate size: 1.5 cm × 3 mm diameter × thickness). d) Scheme depicting the interfacial polymerization of aniline within the binary hybrid hydrogel network. e) Cross-sectional ToF-SIMS analysis of PEGDA/PANI hydrogel. Maps of Cl^- and $C_6H_5NH_2^-$ ions displaying signal intensities along the cross-section of the hydrogel (top and bottom of the gel are indicated with a green dotted line). f) $C_6H_5NH_2^-$ signal normalized to total ion counts over distance.

with a low risk of leakage. The binary hybrid gels were synthesized using a *f*-MoS_2(–OCH_3) loading of 10% w/w compared to PEGDA, while ternary MoS_2/PEGDA/PANI gels were prepared to obtain more conductive specimens. Representative images of the free-standing samples are shown in Figure 3b and c, respectively. The reference binary PEDGA/PANI gel was also produced as a comparison. The conductive polymer was added after the synthesis of the binary hydrogels since PANI particles darkened the mixture and limited UV light penetration, thus interfering with the correct polymerization of PEGDA.[31,54] PANI insertion in the hybrid network was achieved using an interfacial polymerization method.[31] PANI chains formed exclusively inside the PEGDA hydrogel, as the polymerization started at the interface between hexane and the hydrogel and continued toward the bulk, with protonated aniline monomers migrating into the gel internal aqueous phase from the organic solution (where pristine aniline is dissolved). Since PANI is hydrophilic in its acid-doped state, the chains do not grow out of the hydrogel into the organic solvent.[31] Aniline is expected to polymerize both alongside the hydrophilic PEG chains, and also to wrap around the MoS_2 nanoflakes due to π-stacking interactions, as depicted in Figure 3d. FTIR and Raman spectroscopies detected the peaks relative to the formation of the conductive emeraldine salt of PANI (Figure S6a,b, Supporting Information). The main peaks in the IR spectrum are those relative to PEGDA, the main component of the material, so that the characteristic PANI peaks in the range between 500 and ≈2000 cm^{-1} were hidden by those relative, for example, to the stretching of the C═O bond at 1750 cm^{-1}. However, the peak at 1295 cm^{-1} may be indicative of the stretching of the C—N bond (secondary aromatic amine) in the emerald salt of PANI. Moreover, two weak peaks at ≈2330 and 2360 cm^{-1} could be attributed to the stretching of NH^+ in acid-doped PANI.[55] More information about the presence of PANI in the bulk of the composite gel was collected via Raman spectroscopy. The peaks at 1593 cm^{-1} and at 1477 cm^{-1} can be attributed to the stretching vibrations of C═C and C═N bonds in the quinonoid units, respectively.[56,57] The peak at 1348 cm^{-1} was assigned to the stretching vibrations of C—N^+ and that at 1176 cm^{-1} to the C—H bending vibrations of the quinoid units.[56,57]

A qualitative evaluation of the degree of aniline polymerization within the gels was conducted through cyclic voltammetry (CV). Reversible scans of PANI were observed, indicating a high polymerization degree when using long interfacial polymerization time of 16 h (Figure S7a, Supporting Information). Samples with shorter interfacial polymerization times (4 h) exhibited irreversible CVs at different scanning speeds (Figure S7b,c, Supporting Information). This phenomenon stemmed from the undesired electrodeposition of PANI onto the electrode, indicating the presence of unreacted aniline monomers and oligomers within the network after short polymerization times. Indeed, the current density notably increased with subsequent cycles, and the shape of the CV curve drastically changed, reaching a significantly higher current density that remained almost constant across cycles with a preserved shape, suggestive of the formation of a thin layer of PANI[58,59] (Figure S7d, Supporting Information). Hence, it is possible to assume that complete aniline polymerization was obtained after 16 h.

Time-of-flight secondary ion mass spectrometry (ToF-SIMS) analysis was conducted on frozen PEGDA/PANI hydrogels to look for gradients of aniline polymerization throughout the hydrogels. The distribution of PANI was detectable from the $C_6H_5NH_2^-$ mass signal (a mass fragment representing the extremities of the PANI chains) across the thickness of the sample (Figure 3e,f). The count rate dropped drastically when reaching the bottom of the hydrogel (bottom side at around 3 mm), due to the limited diffusion of aniline in proximity to the base of the container. However, the distribution of PANI was notably homogeneous in all other areas of the sample, and the bottom section could be easily removed before using the hydrogel for its final applications. Analysis on MoS_2/PEGDA/PANI hydrogels failed for their high surface roughness determined by MoS_2 nanoflakes.

Data regarding classical hydrogel characterizations, such as the equilibrium swelling ratio (ESR), the equilibrium water content (EWC) and Young's moduli of the different samples are reported in **Table 2** and Figure S8a,b, Supporting Information, and were conducted following the procedure outlined in the Experimental Section. The ESR for the hybrid binary MoS_2/PEGDA hydrogel was lower than that of a pure PEGDA hydrogel, indicating the contribution of the inorganic component on the structural rigidity and hydrophilicity of the material. With the incorporation of PANI, the ESR dropped significantly, indicating an additional contribution of PANI to the structural rigidity of the soft network and the coverage of hydrophilic sites within the matrix. The Young's modulus analysis also strongly supported this hypothesis. The ternary MoS_2/PEGDA/PANI exhibited similar moduli but better reproducibility when compared with the binary MoS_2/PEGDA, hinting at a network stabilizing effect of PANI. The addition of PANI to PEGDA greatly improved the structural properties of the hydrogel with respect to PEGDA alone but at the expense of a larger variability between samples.

The scanning electron microscopy (SEM) images of the freeze-dried PEGDA hydrogels indicated the absence of pores (Figure S9a,b, Supporting Information), attributed to the collapse of the flexible structure. In contrast, the images of the hybrid ternary hydrogels revealed the irregular surface of the material with few microns-sized pores. This porosity resulted from the addition of MoS_2, providing structural stability to the internal microstructure of the hydrogel and limiting its collapse after water removal (Figure S9c,d, Supporting Information). The addition of PANI to form the tertiary hydrogels did not result in significant changes in the material's surface, further supporting the hypothesis that PANI mainly polymerizes in the bulk of

Table 2. Summary of swelling properties and elastic moduli of the ternary MoS_2/PEDGA/PANI hydrogel in comparison to binary references MoS_2/PEDGA and PEGDA/PANI and to pure PEGDA.

Sample name	ESR	EWC [%]	Young's modulus [kPa]
PEDGA	12.5	92.6%	1.59 ± 0.03
MoS_2/PEDGA	10.2	91.1%	3.07 ± 2.53
MoS_2/PEDGA/PANI	6.0	85.7%	3.03 ± 1.05
PEDGA/PANI	5.7	81.4%	14.93 ± 8.85

the network rather than on its surface (Figure S9e,f, Supporting Information).

For the evaluation of the free-standing hydrogel materials as strain sensors, current-voltage (I–V) curves of MoS_2/PEGDA, MoS_2/PEGDA/PANI, PEGDA/PANI under different applied pressures were recorded (see the Experimental Section for detailed protocols). Measurements were recorded at progressively increasing pressures until complete disruption of the sample. The gels containing PANI demonstrated improved mechanical performance, sustaining pressures up to 9.45 kPa, while MoS_2/PEGDA samples tore around 4.25 kPa. The I–V curves showed three distinctive behaviors, as seen from **Figure 4**b,c (MoS_2/PEGDA and MoS_2/PEGDA/PANI) and Figure S10a, Supporting Information (PEGDA/PANI). The MoS_2/PEGDA binary hydrogel displayed the typical behavior of an ohmic resistor, having partially 1T conductive MoS_2 flakes separated by the insulating polymer matrix. The ternary MoS_2/PEGDA/PANI gel showed instead a Schottky-like behavior, likely due to the formation of a heterojunction between MoS_2 and the PANI chains wrapped around it.[60] The curves for the binary PEGDA/PANI had a capacitor behavior with a noticeable offset, mainly due to the capacitive characteristics of PANI itself. The resistance is calculated from the curves applying Ohm's law (Figure 4d,e and S10b, Supporting Information). For the MoS_2/PEGDA/PANI samples, the fitting was performed in the positive bias linear region. All hydrogels containing PANI demonstrated significantly lower resistance of the unloaded samples compared to MoS_2/PEGDA. Both MoS_2/PEGDA and MoS_2/PEGDA/PANI showed a measurable decrease in resistance with increasing pressure, indicating the ability to distinguish strains of different intensities. PEGDA/PANI hydrogels had a similar trend only at the lowest pressures up to 1.65 kPa. Such behavior is a strong indication of the anisotropic effect provided by the 2D TMD nanoflakes in the network, which induce a progressively higher overall conductance by arranging from a random nanoscale distribution toward a flattened (2D) and more uniform disposition as a function of the increased external pressure.

Current-strain curves showed similar behaviors, with samples containing MoS_2 presenting an almost linear increase in current with increasing strain, whereas PEGDA/PANI hydrogels quickly lost linear behavior after 30% strain (Figure 4f). Taken together, these results confirmed that the bidimensional MoS_2 enabled a piezoresistive response in the hybrid hydrogel.[17] With compression, the hydrogel matrix deforms, reducing the spacing between the embedded MoS_2 flakes and creating contact points between them, as depicted in Figure 4a. Edge or basal plane contact generates new conductive pathways and therefore decreases the resistance of the material.[18,61,62] Interestingly, the ranges where we measured strain sensing abilities were within the order of magnitude of physiological vascular pressures. Specifically, 0.8 and 9.45 kPa correspond to approximately 6 and 70 mmHg, respectively, values representative of the vascular pressures of arterioles and veins.

Chronoamperometry further allowed to assess the stability of the hybrid free-standing gels, by loading and unloading the samples with weight over time. The current response, reported as $\Delta I/I_0$, where I_0 is the current measured for the unloaded sample, exhibited good stability over time at lower pressures, indicating that the samples could function as strain sensors for prolonged periods of at least 380 s. All samples displayed larger increases in current at higher pressures (Figure 4g, S10, Supporting Information). A slight decrease in current over time was observed for MoS_2/PEGDA, likely due to its lower structural rigidity which could lead to a permanent deformation of the network (Figure S10c, Supporting Information). The ternary hydrogel confirmed its improved structural stability resulting from the incorporation of PANI. This sample showed the highest current response with pressure ($\Delta I/I_0 \approx 500$, Figure 4g), ensuring an excellent performance for its use in a strain sensor device. PEGDA/PANI showed a similar behavior but with a less reproducible current response over time and slight hysteresis (Figure S10d, Supporting Information).

In sight of a potential application of these hybrid materials as pressure-sensing components within wearable devices, we also evaluated the responses of living cells following direct contact with the hydrogels. These tests can provide critical insights into the possible interactions of the material with biological systems at a cellular level, in a simplified in vitro system that however retains some characteristics of its in vivo counterpart. For this purpose, small cylindrical samples ("pillars") were encapsulated within cellularized gelatin methacrylate (GelMA) scaffolds and analyzed after 7 d in culture. Given the intended application, human fibroblasts (BJ cells) were chosen as a proxy of the epithelial environment where our hybrid materials would be applied. Moreover, the encapsulation within GelMa simulated the final design of device composed of our sensing material enclosed in a highly biocompatible environment. Cell responses were evaluated with a Live/Dead analysis using three specific fluorescent markers: Calcein-AM (staining the cytoplasm of live cells green), Hoechst (staining all cell nuclei blue), and Propidium iodide (staining the nuclei of dead cells red). The semi-quantitative evaluation of the fluorescent signals on day 7 showed high cell viability without significant differences among groups (Figure S11, Supporting Information). Visualization of the green florescent signal marking the cytoplasm of live cells also proved their uniform distribution and consistent viability throughout the 3D construct, including, and most importantly, when in close proximity with the PEGDA/PANI, MoS_2/PEGDA/PANI, and MoS_2/PEGDA pillars. The cell distribution and viability were also comparable in control samples containing only PEGDA. **Figure 5** and S11, Supporting Information, report representative images from the Live/Dead assay. A semi-quantitative image analysis calculated an average viability of 98% across all composite hydrogels. This value is comparable to the viability of cellularized GelMA samples without the inclusion of the hydrogel pillars, thus confirming their biocompatibility. The use of biocompatible materials such as PEGDA and the inclusion of conductive polymers like PANI do not adversely affect the cells, making these materials promising for biomedical applications. In addition, the uniform distribution and consistent viability of the cells throughout the 3D construct, including near the hydrogel pillars, indicate that the hydrogels do not hinder cell growth or distribution. The absence of significant differences in viability among the different hydrogel formulations suggests that the modifications made to improve the hydrogels' mechanical and electrical properties do not compromise their biocompatibility. Given the high biocompatibility and the excellent mechanical properties of these hybrid

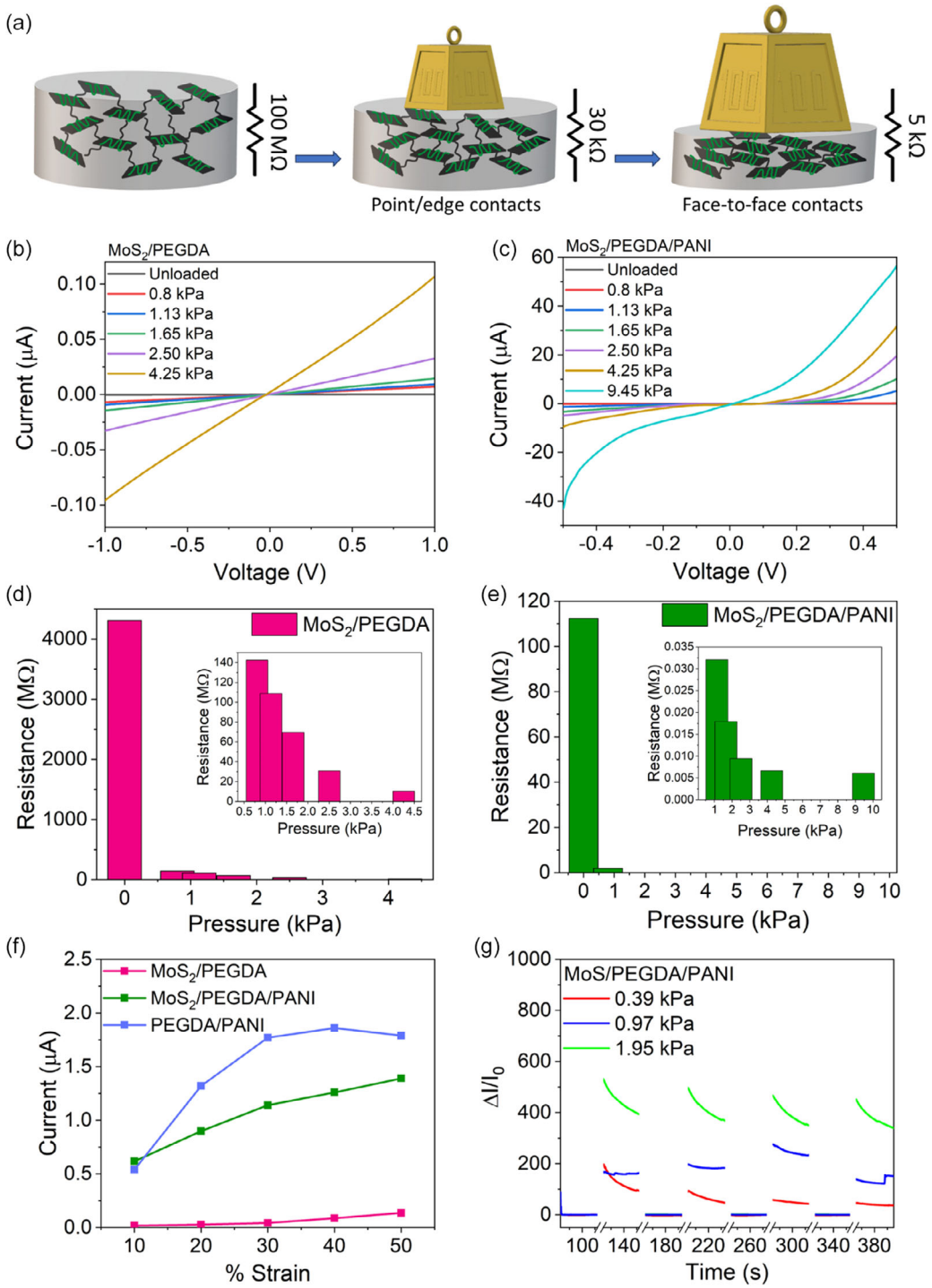

Figure 4. Evaluation of the piezoresistive behavior of hybrid hydrogels. a) Schematic illustration of the piezoresistive sensing mechanism with the increase of external pressure. b,c) *I–V* characteristics and d,e) resistance trends of, respectively, MoS_2/PEGDA and MoS_2/PEGDA/PANI free-standing hydrogels as a function of the applied pressure (weights displaced on top of the gel surface and current measured at the bottom by disposing the samples on gold electrode substrates). f) Current–strain curves for the three samples and g) chronoamperometric data for MoS_2/PEGDA/PANI hydrogel.

hydrogels, they hold significant potential for use in wearable and implantable devices. The materials' ability to maintain high cell viability while providing enhanced electrical and mechanical properties makes them suitable for applications in bioelectronics, such as sensors and actuators that interact directly with biological tissues. The use of GelMA as an encapsulating

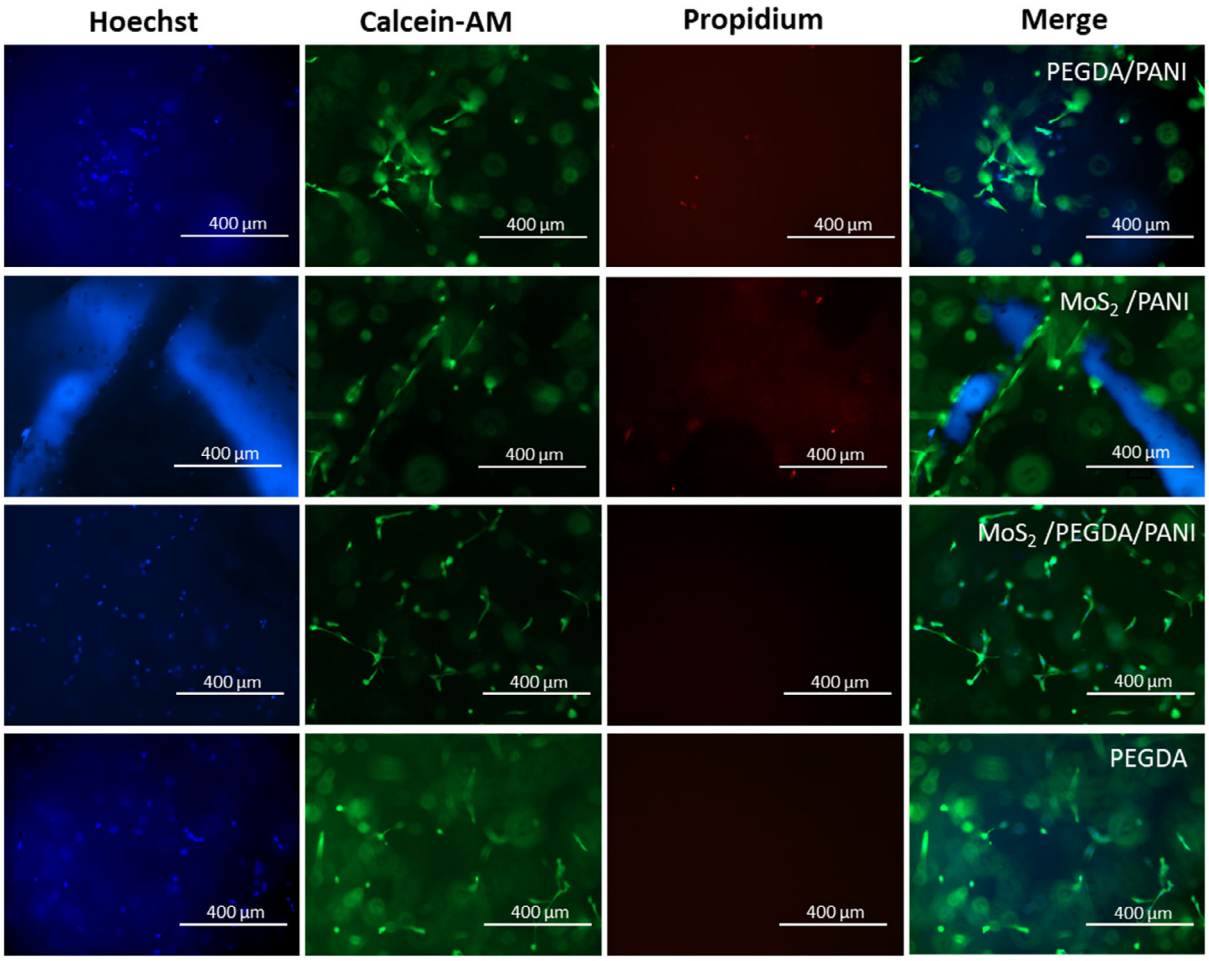

Figure 5. Cell viability analyzed by the Live/Dead assay at day 7 for BJ cells. Hoechst stains nuclei of all cells in blue, Calcein-AM stains live cells in green, and propidium stains dead cells in red. Scale bars 400 µm.

material simulates the final design of the device, where the sensing material would be enclosed in a highly biocompatible environment. This experimental setup provides a realistic evaluation of how these materials would perform in practical biomedical applications. The results encourage further exploration of these hybrid hydrogels for various biomedical applications. Future research could focus on long-term biocompatibility studies, in vivo testing, and the development of specific devices incorporating these materials for real-time health monitoring and other biomedical applications.

3. Conclusions

In summary, this study presents a piezoresistive, covalently cross-linked hydrogel based on 2D MoS_2, with improved conductivity thanks to interfacial polymerization of aniline. The introduction of aryl moieties on the surface of MoS_2 *via* Tour reaction allows the creation of chemical crosslinks between PEGDA and the nanoflakes, effectively limiting the migration of nanomaterial outside of the hydrogel matrix.

The subsequent incorporation of PANI serves a dual purpose within the hybrid material: enhancing its mechanical properties while simultaneously boosting the overall conductivity of the hydrogel. This enables more accurate detection of signal fluctuations, making the material more suited for prospective applications in wearable strain-sensing devices. In summary, the process results in a ternary MoS_2/PEGDA/PANI hydrogel, which benefits from the anisotropy introduced by the two-dimensional material, enabling it to detect strain stimuli effectively and the substantial effects of PANI on the electrical conductivity and the mechanical stability. Electromechanical tests show that hydrogels containing few-layers MoS_2 feature a significant decrease in resistance with increasing compressive strain. This behavior is given by the reduced spacing between the flakes in the network, creating more conductive pathways with increasing pressure. As counterproof, it is shown that a hydrogel containing PANI and no 2D material does not perform in a similar manner. Stability tests with continuous loading and unloading were also performed, demonstrating the potential for these materials to be used in wearable devices for real-time monitoring of physiological stimuli.

A feasible target application could be blood pressure monitoring, considering the pressure range used for the characterization of their piezoresistive behavior. Biocompatibility tests in vitro demonstrated that the inclusion of the different hydrogel formulations within a 3D cellularized construct does not compromise cell viability, supporting their use in a biological setting. Beyond biocompatibility, the mechanotransductive potential of these hybrid hydrogels offers additional avenues for application in wearable and implantable devices. Mechanotransduction, the process by which cells convert mechanical stimuli into biochemical signals, can be harnessed to enhance cellular responses within the hydrogel matrix. The MoS_2/PEGDA/PANI hydrogels, with their tunable mechanical properties and electrical conductivity, provide a unique platform for stimulating cellular mechanotransductive pathways. By mimicking the natural mechanical environment of tissues, these hydrogels can promote processes such as cell proliferation, differentiation, and tissue regeneration, making them particularly valuable for tissue engineering applications. Moreover, the sensitivity of these materials to mechanical deformation enables their use in wearable sensors for real-time health monitoring, where they can detect physiological parameters like heart rate and blood pressure through mechanical cues. Thus, integrating mechanotransductive capabilities into these hydrogels not only enhances their functionality but also opens up new possibilities for advanced biomedical applications, further validating their potential as innovative materials in the field of bioelectronics and regenerative medicine.

Such a soft scaffold, rigid enough to be fully self-standing and pressure-tunable anisotropic electrical resistance, proves to be a promising material to be used in the emerging field of wearable electronics. This sector is projected to significantly expand in the near future, making materials like these valuable contributors to technological advancements.

4. Experimental Section

Materials: MoS_2 2 μm powder (98%), p-anisidine (99%), polyethylene glycol diacrylate (MW: 700), aniline (for synthesis), n-butyllithium (2.5 M in dry hexane), isopentyl nitrite (96%), sodium dodecyl sulfate (>98%), and N-Methyl-2-pyrrolidone were purchased from Sigma Aldrich and used without further purification. 1-hydroxycyclohexyl phenyl ketone (Irgacure 184) was purchased from Alfa Aesar and used without further purification.

1T-MoS_2 Exfoliation: 1 g of bulk MoS_2 (6.25 mmol) was dried for 1 h under vacuum with mild heating (40 °C) and agitation in a pre-dried round-bottle flask connected to a Schlenk line. 6 mL of 2.5 M n-butyl lithium (15 mmol, 2.4 eq) were then added under Argon flux. The solution was stirred at 40 °C in Argon atmosphere for 3 d. After the reaction time, the mixture was retrieved first under Argon flux using hexane, then centrifuged using a Universal 320 Hettich centrifuge at 7000 rpm (4650 g) for 12 min 3–5 times with fresh hexane until the remaining suspension was clear. The obtained powder was dried in a vacuum oven at 40 °C for 1 h. The powder was then dispersed in an appropriate amount of water at a concentration of 2 mg mL^{-1}. The suspension was then placed in an ice bath and sonicated using a Bandelin Sonoplus tip sonicator at 80% power output for 2 h, changing the ice bath after the first hour. The final ink was then centrifuged once at 6000 rpm (3427 g) for 20 min and the supernatant transferred into a clean bottle. Whenever necessary, the ink was freeze dried using a Martin Christ Alpha 2–4 LD plus freeze dryer to obtain 2D-MoS_2(1T) powder.

2D-MoS_2(1T) Functionalization with Diazonium Salts: 50 mg of 2D-MoS_2(1T) were dispersed in 50 mL of NMP in a two-necked round bottom flask using an ultrasonic bath. 19.70 mg of p-anisidine (0.16 mmol, 0.5 eq) were then added. The suspension was heated to 80 °C under reflux while stirring. Once the desired temperature was reached, 20.80 μL of isopentyl nitrite (0.31 mmol, 1 eq.) were added. The mixture was stirred for 4 h. The suspension was allowed to cool down at room temperature for 20 min, after which 100 mL of fresh acetone were added. The suspension was then filtered on an Omnipore PTFE filter (0.2 μm pore cut off) and washed first with 10 mL of NMP and then twice with 10 mL of fresh acetone. The powder was then extracted from the filter by dispersing the material in isopropanol using an ultrasonic bath. The isopropanol was then removed using a rotary evaporator.

PEGDA-Based Gel Production: PEGDA based gels were produced by mixing 50 mg of the polymeric precursor and 5 mg of initiator (Irgacure 184) in a 12 mm diameter PTFE mold with 1 mL of distilled water. The solution was stirred at 40 °C for 30 min. Once the solution was clear, it was placed under a Hartmann UV-P 250 C7S UV lamp for 30 min, leading to the formation of a compact transparent gel. A similar protocol was followed for *f*-MoS_2/PEGDA gels, where the same precursors were dissolved in 0.5 mL of distilled water, while 5 mg of the functionalized material was sonicated in 0.5 mL of water. After this step, the polymeric precursor solution was combined with the functionalized material solution and stirred for 30 min. The mixture was then polymerized under a UV lamp using the same conditions. The as-obtained gel was dark colored.

PANI Impregnation of PEGDA-Based Gels: The confined-space PANI impregnation was performed by first immersing the desired gels into a 1 M HCl solution containing 50 mg of $K_2S_2O_8$ (0.18 mmol, 1.5 eq) for 2 h. The gels were then immersed in a 0.025 M Aniline solution in hexane for 16 h, after which they were removed from and washed first by immersion in 1 M HCl for 1 h and then in distilled water for another hour.

Materials Characterization: UV-Vis spectroscopy was performed on a Uvikon spectrometer, using QS High Precision Cells made of Quartz Suprasil by Hellma Analytics with a light path of 10 mm. Raman spectra were collected at room temperature using a Bruker Senterra R200-532 spectrometer, using a 532 nm laser and using 50 times magnification. The spectra were collected using the following instrumental settings: 5 s of integration time, 60 co-addition and a laser power of 2 mW. Samples were observed in HRTEM with a non-aberration corrected Transmission Electron Microscope (TALOS F200X, ThermoScientific, Eindhoven, Netherland) operated at 200 kV. Images were recorded on a 16Mpxls CMOS camera with 1 s exposure time. Zeta potential measurements were performed with a Nano ZS Zetasizer system (Malvern Instruments), using a 633 nm laser wavelength, and a refracting index of 4.08 for MoS_2. FT-IR was performed using a DRIFT (Diffuse Reflectance Infrared Fourier) Bruker Alpha spectrometer measuring in the range 40–4000 cm^{-1} with 48 co-additions for each measurement. Thermo-gravimetric analysis (TGA) was performed using an automized NETZSCH STA 409 from Erich NETZSCH GmbH & Co. The measurements were performed in inert atmosphere (Ar) in the range from room temperature to 900 °C with a heating ramp of 10 °C min^{-1}. X-Ray Photoelectron spectra were collected using a PHI5000 VersaProbe IV Scanning ESCA Microscope (Physical Electronics) with a monochromatized Al Kα X-ray source (beam diameter: 100 μm, nominal X-Ray power: 25 W). The spectra were collected under Argon ions neutralization and in a vacuum between 10^{-6} and 10^{-7} Pa and using a pass energy of 112 eV for the Survey and 27 eV for the detailed scans, for 30 sweeps or when the P/N ratio of 180 was reached. Data were analyzed using the CasaXPS software; fitting was performed using a GL(00)T(1.1) function with a Shirley background. Calibration of the spectra lines was performed using the C 1s peak at 284.8 eV. Imaging mass spectrometric investigations were carried out with a M6 Hybrid SIMS (IONTOF GmbH, Muenster, Germany. 1 mm thick cross sections of the hydrogels were cut using a razor blade and placed on a cryo sample holder. The samples were purged for 5 min in the loadlock chamber with dry nitrogen at a pressure of 750 mbar before being cooled down to −40 °C. At this temperature, we started the pumping system and transferred the samples in the main analysis chamber at −40 °C. Here the samples were cooled to −149 °C for measurement. For charge compensation, the low energetic flood gun was used, and the chamber pressure increased to 10^{-6} mbar by introducing Ar via the gas nozzle. Mass spectrometric imaging was carried out with 30 keV Bi^{3+} primary ions.

The mounted nanoprobe 50 was operated in spectrometry mode with a beam defining aperture of 700 µm resulting in a current of 0.89 pA @ 80 µs cycle time. Stage scans of an area of 0.8×3.2 mm^2 were carried out with a pixel density of 200 Pi/mm, 50 frames/patch. The dose density was 5.28×10^{11} cm^{-2} within static limit. The analyzer was operated in all-purpose mode with topography functionality.

Electromechanical Testing: The electromechanical response of gels was characterized by stepped compression tests on an Instron 3365 dynamometer equipped with a 10 N load cell, coupled with current measurements on a Keithley 2621B Sourcemeter. Tests were composed by two consecutive routines: in the first, samples were subjected to loading with the rate of 2 mm min^{-1} until a strain of 30% was reached. From this loading phase, Young's modulus was calculated as the slope of the stress-strain curve. Displacement was then held at 30% for 30 s and released with the same rate until the load of 50 mN, where the position was again held for 30 s for stress relaxation. From there, load was increased stepwise with 10% strain steps until 50%. At each step, the position was held for 30 s. Throughout the test, 1 V tension was applied to the sample through electrodes on the top and bottom surfaces and the corresponding current was measured. Probe station measurements were carried out with a Keithley Parameter Analyzer 4200-SCS, performing a voltage sweep scanning from −10 to 10 V, or from −0.5 to 0.5 V. The gels were cut to a cylindrical shape 6 mm diameter and 2 mm thickness and placed onto a Metrohm DropSens 250AT screen-printed gold electrode with a platinum auxiliary electrode. The two probes were contacted on the gold and platinum electrode, respectively. Additional weight was placed onto the gels before each scan. Cyclic voltammetry and chronoamperometry were performed using an Autolab PGSTAT302 potentiostat equipped with the Nova (2.1.1.) software. For CV scans, cylindrical hydrogels were placed onto a glassy carbon (GC) electrode, and a PTFE cylindrical cap was used to press the hydrogel on the electrode to secure contact. The electrochemical cell was set up using GC as working electrode (WE), Pt wire as counter electrode (CE), Ag/AgCl electrode as reference electrode (RE). The measurements were performed in a 1 M H_2SO_4 solution (pH − 0.3) at room temperature. Scans were performed from −1 to 1 V at scanning speeds of 5, 10, 25, 50, and 100 mV s^{-1}. The WE potentials were converted to be referred to the reversible hydrogen electrode (RHE). For CA scans, the gels were placed on a Metrohm DropSens 250AT screen-printed gold electrode with a platinum auxiliary electrode. The measurements were performed at applied 0 V, for 30 s, with a 10 s pause between each measurement to load and unload weights on the sample.

GelMA Preparation: The hydrogel used for the cellularized constructs was a solution of GelMA (8% w/v) and Irgacure 2959 (0.5% w/v) (Sigma-Aldrich) in 1xPBS. GelMa was prepared following the procedure described in Bova et al.[57] The photoinitiator was dissolved in warm 1xPBS (40 °C) for 20 min with constant stirring (800 rpm), then the solution was filtered (0.22 µm filters) into 50 mL Falcon tubes containing the lyophilized GelMA. The mixture was kept at 37 °C with occasional vortexing until complete GelMA dissolution. Before use, the hydrogel was centrifuged to remove all air bubbles (3500 rpm, 5 min).

Cell Culture and Hydrogels Preparation: The human skin cell line (BJ, ATCC) was cultured using Eagle's Minimum Essential Medium (EMEM, ATCC) with 10% FBS and 1% P/S. Cells were maintained in an incubator at 37 °C in a humidified atmosphere with 5% CO_2. Prior to seeding, the different hydrogels (PEGDA/PANI, MoS_2/PEGDA, MoS_2/PEGDA/PANI and PEGDA) were cut into small pillars using a biopsy punch with a diameter of 2 mm. They were then washed twice with phosphate buffered saline (PBS) to remove residual contaminants and possible debris. Following the preparation steps, the hydrogels were incubated at 37 °C for 1 h in a 96-well plate pre-conditioned with fresh culture medium. This pre-conditioning was essential to prime the scaffold substrates for optimal cell adhesion and growth.

Encapsulation of Cells in Composite Hydrogels: BJ cells were detached from the flask by trypsinization (0.25% trypsin/EDTA) and resuspended in an appropriate volume of medium. The volume for resuspension was calculated to yield a final cell density of 1.5 million BJ per mL of hydrogel. Once resuspended, the cells were mixed with the sterile GelMA by gentle pipetting. Cylindrical samples of cellularized GelMA were obtained by casting in autoclaved PDMS molds. The small hydrogel pillars were encapsulated by distributing them on the GelMA bulk prior to UV polymerization. The constructs were bathed in 3 mL of cell culture medium, which was replaced after the first 24 h and then every other day.

Cell Viability Assay: To evaluate cell viability, a Live/Dead assay was conducted on the constructs after 7 d from seeding. Cells were stained with a solution of Hoechst (1:500 dilution, Sigma-Aldrich, St. Louis, MO, USA), Calcein-AM (1:1000, Sigma-Aldrich, St. Louis, MO, USA), and Propidium Iodide (1:500, Sigma-Aldrich, St. Louis, MO, USA) in PBS for 45 min at 37 °C in the dark. Images were acquired on a fluorescence microscope (EVOS Flois Imaging System) and analyzed with the "Analyze particles" tool of ImageJ software. Automated cell counting enabled the quantification of living cells over the total number of cells, as a measure of cell viability. Cell counting was repeated on at least 10 images.

Supporting Information

Supporting Information is available from the Wiley Online Library or from the author.

Acknowledgements

The authors acknowledge the financial support of the European Commission through the H2020 FET-PROACTIVE-EIC-07-2020 project LIGHT-CAP (grant agreement no. [101017821]) and of the European Research Council through the ERC StG project JANUS BI (grant agreement no. [101041229]). We also thank the NODES Ecosystem (Nord Ovest Digitale e Sostenibile), funded by the NextGenerationEU scheme, for financial support through the PoC project HYSENS. M.R. thanks the DFG for funding of the Hybrid-SIMS (M6 Hybrid SIMS, IONTOF GmbH, Muenster, Germany) under grant number INST 162/544-1 FUGG. S.D. would like to thank Juri Becker and Pascal Schweitzer for the essential help creating a self-made setup for the electromechanical stability tests.

Conflict of Interest

The authors declare no conflict of interest.

Data Availability Statement

The data that support the findings of this study are available from the corresponding author upon reasonable request.

Keywords

2D MoS_2, covalent functionalization, PANI, PEGDA hydrogel, piezoresistive pressure sensor

Received: March 21, 2024
Revised: May 16, 2024
Published online: June 13, 2024

[1] Z. Wang, H. Song, L. Chen, W. Li, D. Yang, P. Cheng, H. Duan, *ACS Appl. Electron. Mater.* **2022**, *4*, 5199.
[2] Z. Chen, Y. Chen, M. S. Hedenqvist, C. Chen, C. Cai, H. Li, H. Liu, J. Fu, *J. Mater. Chem. B* **2021**, *9*, 2561.
[3] J. Cho, *J. Healthcare Eng.* **2019**, *2019*, 3924508.
[4] Y. W. Chong, W. Ismail, K. Ko, C. Y. Lee, *IEEE Sens. J.* **2019**, *19*, 9047.

[5] K. Guk, G. Han, J. Lim, K. Jeong, T. Kang, E. K. Lim, J. Jung, *Nanomaterials* **2019**, *9*, 813.
[6] A. Ometov, V. Shubina, L. Klus, J. Skibińska, S. Saafi, P. Pascacio, L. Flueratoru, D. Q. Gaibor, N. Chukhno, O. Chukhno, A. Ali, A. Channa, E. Svertoka, W. Bin Qaim, R. Casanova-Marqués, S. Holcer, J. Torres-Sospedra, S. Casteleyn, G. Ruggeri, G. Araniti, R. Burget, J. Hosek, E. S. Lohan, *Comput. Networks* **2021**, *193*, 108074.
[7] J. Xie, Q. Chen, H. Shen, G. Li, *J. Electrochem. Soc.* **2020**, *167*, 037541.
[8] E. Feng, W. Gao, Z. Yan, J. Li, Z. Li, X. Ma, L. Ma, Z. Yang, *J. Power Sources* **2020**, *479*, 229100.
[9] Y. Cai, J. Shen, C.-W. Yang, Y. Wan, H.-L. Tang, A. A. Aljarb, C. Chen, J.-H. Fu, X. Wei, K.-W. Huang, Y. Han, S. J. Jonas, X. Dong, V. Tung, *Sci. Adv.* **2020**, *6*, eabb5367.
[10] Q. Ling, T. Ke, W. Liu, Z. Ren, L. Zhao, H. Gu, *Ind. Eng. Chem. Res.* **2021**, *60*, 18373.
[11] F. Lamberti, S. Giulitti, M. Giomo, N. Elvassore, *J. Mater. Chem. B* **2013**, *1*, 5083.
[12] G. Ge, Y. Zhang, J. Shao, W. Wang, W. Si, W. Huang, X. Dong, *Adv. Funct. Mater.* **2018**, *28*, 1802576.
[13] D. Zhang, B. Ren, Y. Zhang, L. Xu, Q. Huang, Y. He, X. Li, J. Wu, J. Yang, Q. Chen, Y. Chang, J. Zheng, *J. Mater. Chem. B* **2020**, *8*, 3171.
[14] S. Boon-in, M. Theerasilp, D. Crespy, *J. Colloid Interface Sci.* **2022**, *622*, 75
[15] S. Zhao, B. Dong, H. Wang, H. Wang, Y. Zhang, Z. V. Han, H. Zhang, *Nanoscale Adv.* **2020**, *2*, 109.
[16] T. Liu, Z. Liu, *Adv. Healthcare Mater.* **2018**, *7*, 1701158.
[17] Y. Yue, N. Liu, W. Liu, M. Li, Y. Ma, C. Luo, S. Wang, J. Rao, X. Hu, J. Su, Z. Zhang, Q. Huang, Y. Gao, *Nano Energy* **2018**, *50*, 79.
[18] Y.-Z. Zhang, K. Hyuck Lee, D. H. Anjum, R. Sougrat, Q. Jiang, H. Kim, H. N. Alshareef, *Sci. Adv.* **2018**, *4*, eaat0098.
[19] S. N. Li, Z. R. Yu, B. F. Guo, K. Y. Guo, Y. Li, L. X. Gong, L. Zhao, J. Bae, L. C. Tang, *Nano Energy* **2021**, *90*, 106502.
[20] Q. Y. Ni, X. F. He, J. L. Zhou, Y. Q. Yang, Z. F. Zeng, P. F. Mao, Y. H. Luo, J. M. Xu, B. Jiang, Q. Wu, B. Wang, Y. Q. Qin, L. X. Gong, L. C. Tang, S. N. Li, *J. Mater. Sci. Technol.* **2024**, *191*, 181.
[21] S. N. Li, X. F. He, Z. F. Zeng, B. Jiang, Q. Wu, L. X. Gong, Y. Li, J. Bae, S. Wang, L. C. Tang, *Nano Energy* **2022**, *103*, 107789.
[22] V. Yadav, S. Roy, P. Singh, Z. Khan, A. Jaiswal, *Small* **2019**, *15*, e1803706.
[23] L. Zapór, L. Chojnacka-Puchta, D. Sawicka, K. Miranowicz-Dzierzawska, J. Skowroń, *Nanotechnol. Rev.* **2022**, *11*, 1263.
[24] W. Z. Teo, E. L. K. Chng, Z. Sofer, M. Pumera, *Chem. – Eur. J.* **2014**, *20*, 9627.
[25] S. Pinilla, J. Coelho, K. Li, J. Liu, V. Nicolosi, *Nat. Rev. Mater.* **2022**, *7*, 717.
[26] C. Backes, T. M. Higgins, A. Kelly, C. Boland, A. Harvey, D. Hanlon, J. N. Coleman, *Chem. Mater.* **2017**, *29*, 243.
[27] W. Xu, W. Wang, S. Chen, R. Zhang, Y. Wang, Q. Zhang, L. Yuwen, W. J. Yang, L. Wang, *J. Colloid Interface Sci.* **2021**, *586*, 601.
[28] P. Shah, T. N. Narayanan, C. Z. Li, S. Alwarappan, *Nanotechnology* **2015**, *26*, 315102.
[29] J. Pan, X. Zhou, H. Gong, Z. Lin, H. Xiang, X. Liu, X. Chen, H. Li, T. Liu, S. Liu, *ACS Appl. Mater. Interfaces* **2023**, *15*, 36636.
[30] X. Y. Tao, Y. Wang, W. B. Ma, S. F. Ye, K. H. Zhu, L. T. Guo, H. L. Fan, Z. S. Liu, Y. B. Zhu, X. Y. Wei, *J. Mater. Sci.* **2021**, *56*, 16028.
[31] Y. Wu, Y. X. Chen, J. Yan, S. Yang, P. Dong, P. Soman, *J. Mater. Chem. B* **2015**, *3*, 5352
[32] X. F. He, Z. F. Zeng, Q. Y. Ni, Z. C. Xu, P. F. Mao, B. Jiang, Q. Wu, B. Wang, L. X. Gong, L. C. Tang, S. N. Li, *Composites, Part B* **2023**, *266*, 111022.
[33] K. C. Knirsch, N. C. Berner, H. C. Nerl, C. S. Cucinotta, Z. Gholamvand, N. McEvoy, Z. Wang, I. Abramovic, P. Vecera, M. Halik, S. Sanvito, G. S. Duesberg, V. Nicolosi, F. Hauke, A. Hirsch, J. N. Coleman, C. Backes, *ACS Nano* **2015**, *9*, 6018.
[34] R. D. Pyarasani, T. Jayaramudu, A. John, *J. Mater. Sci.* **2019**, *54*, 974.
[35] P. Humpolíček, V. Kašpárková, J. Pacherník, J. Stejskal, P. Bober, Z. Capáková, K. A. Radaszkiewicz, I. Junkar, M. Lehocký, *Mater. Sci. Eng. C* **2018**, *91*, 303.
[36] P. Vishnoi, A. Sampath, U. V. Waghmare, C. N. R. Rao, *Chem. – Eur. J.* **2017**, *23*, 886.
[37] Z. Lei, J. Zhan, L. Tang, Y. Zhang, Y. Wang, *Adv. Energy Mater.* **2018**, *8*, 1703482.
[38] D. O. Li, M. S. Gilliam, X. S. Chu, A. Yousaf, Y. Guo, A. A. Green, Q. H. Wang, *Mol. Syst. Des. Eng.* **2019**, *4*, 962.
[39] M. Lihter, M. Graf, D. Iveković, M. Zhang, T. H. Shen, Y. Zhao, M. Macha, V. Tileli, A. Radenovic, *ACS Appl. Nano Mater.* **2021**, *4*, 1076.
[40] J. L. Bahr, J. M. Tour, *Chem. Mater.* **2001**, *13*, 3823.
[41] K. Hernandez Ruiz, Z. Wang, M. Ciprian, M. Zhu, R. Tu, L. Zhang, W. Luo, Y. Fan, W. Jiang, *Small Sci.* **2022**, *2*, 2100047.
[42] E. Er, H. L. Hou, A. Criado, J. Langer, M. Möller, N. Erk, L. M. Liz-Marzán, M. Prato, *Chem. Mater.* **2019**, *31*, 5725.
[43] S. Kaushik, S. S. Nemala, M. Kumar, D. Negi, B. Dhal, L. Saini, R. Banavath, S. Saha, S. Sharma, G. Kalon, *Nano-Struct. Nano-Objects* **2022**, *32*, 100922.
[44] S. K. Mahatha, K. D. Patel, K. S. R. Menon, *J. Phys.: Condens. Matter* **2012**, *24*, 475504.
[45] X. Geng, W. Sun, W. Wu, B. Chen, A. Al-Hilo, M. Benamara, H. Zhu, F. Watanabe, J. Cui, T. P. Chen, *Nat. Commun.* **2016**, *7*, 10672.
[46] S. Manjunatha, S. Rajesh, P. Vishnoi, C. N. R. Rao, *J. Mater. Res.* **2017**, *32*, 2984.
[47] F. Liu, Y. Zou, X. Tang, L. Mao, D. Du, H. Wang, M. Zhang, Z. Wang, N. Yao, W. Zhao, M. Bai, T. Zhao, Y. Liu, Y. Ma, *Adv. Funct. Mater.* **2022**, *32*, 2204601.
[48] H. Li, H. Li, Z. Wu, L. Zhu, C. Li, S. Lin, X. Zhu, Y. Sun, *J. Mater. Sci. Technol.* **2022**, *123*, 34.
[49] L. Daukiya, J. Teyssandier, S. Eyley, S. El Kazzi, M. C. Rodríguez González, B. Pradhan, W. Thielemans, J. Hofkens, S. De Feyter, *Nanoscale* **2021**, *13*, 2972.
[50] X. S. Chu, A. Yousaf, D. O. Li, A. A. Tang, A. Debnath, D. Ma, A. A. Green, E. J. G. Santos, Q. H. Wang, *Chem. Mater.* **2018**, *30*, 2112.
[51] K. Sampathkumar, V. Diez-Cabanes, P. Kovaricek, E. Del Corro, M. Bouša, J. Hošek, M. Kalbac, O. Frank, *J. Phys. Chem. C* **2019**, *123*, 22397.
[52] I. Gómez-Muñoz, S. Laghouati, R. Torres-Cavanillas, M. Morant-Giner, N. V. Vassilyeva, A. Forment-Aliaga, M. Giménez-Marqués, *ACS Appl. Mater. Interfaces* **2021**, *13*, 36475.
[53] V. Mévellec, S. Roussel, L. Tessier, J. Chancolon, M. Mayne-L'Hermite, G. Deniau, P. Viel, S. Palacin, *Chem. Mater.* **2007**, *19*, 6323.
[54] V. Guarino, M. A. Alvarez-Perez, A. Borriello, T. Napolitano, L. Ambrosio, *Adv. Healthcare Mater.* **2013**, *2*, 218.
[55] S. Ghatak, G. Chakraborty, A. K. Meikap, T. Woods, R. Babu, W. J. Blau, *J. Appl. Polym. Sci.* **2011**, *119*, 1016.
[56] Q. Chen, X. Miao, Y. Liu, X. Zhang, S. Chen, Z. Chen, Y. Chen, J. Lin, Y. Zhang, *Electrochim. Acta* **2021**, *390*, 138819.
[57] R. Hu, J. Zheng, *J. Power Sources* **2017**, *364*, 200.

[58] Y. B. Shim, M. S. Won, S. M. Park, *J. Electrochem. Soc.* **1990**, *137*, 538.
[59] W. Meng, Y. Xia, C. Ma, X. Du, *Polymers* **2020**, *12*, 2303.
[60] X. Tian, X. Cui, Y. Xiao, T. Chen, X. Xiao, Y. Wang, *ACS Appl. Mater. Interfaces* **2023**, *15*, 9604.
[61] Y. Lu, X. Qu, W. Zhao, Y. Ren, W. Si, W. Wang, Q. Wang, W. Huang, X. Dong, *Research* **2020**, *2020*, 2038560.
[62] L. Bova, F. Maggiotto, S. Micheli, M. Giomo, P. Sgarbossa, O. Gagliano, D. Falcone, E. Cimetta, *Macromol. Biosci.* **2023**, *23*, 2200357.